Cell Reports

Report

Loss of Myelin Basic Protein Function Triggers Myelin Breakdown in Models of Demyelinating Diseases

Graphical Abstract

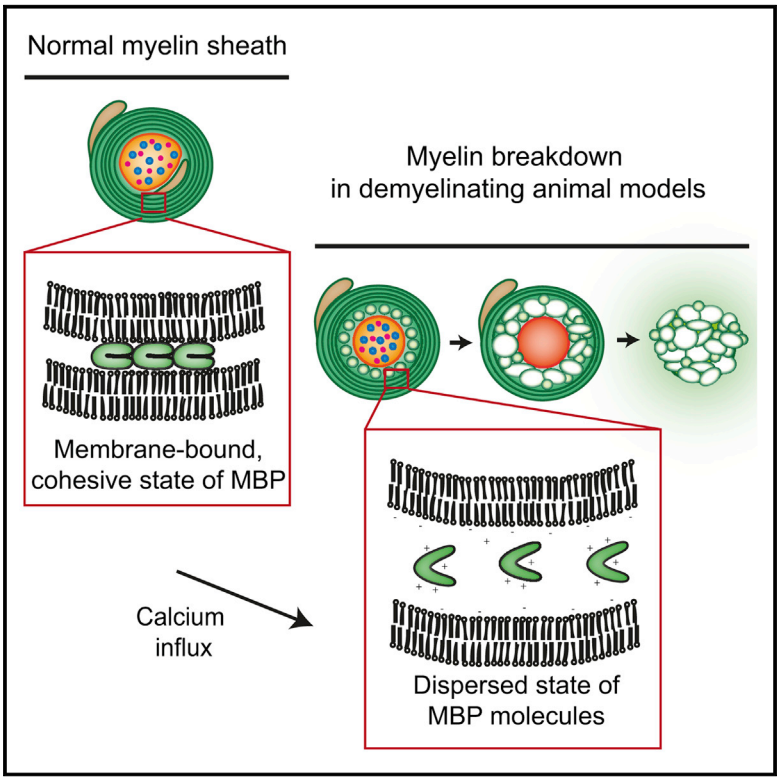

Authors

Marie-Theres Weil, Wiebke Möbius, Anne Winkler, ..., Nicole Schaeren-Wiemers, Christine Stadelmann, Mikael Simons

Correspondence

msimons@gwdg.de

In Brief

Using high-pressure freezing and electron microscopy, Weil et al. show that that the vesicular disruption of the myelin sheath is a common feature of myelin degeneration in demyelinating diseases. The authors suggest that the underlying mechanism is the aberrant transition of MBP molecules from their cohesive state to their non-adhesive state.

Highlights

- Characterization of myelin sheath pathology close its native state
- Vesiculation of inner sheath layers is a common feature of myelin pathology
- Loss of MBP function triggers myelin vesiculation
- Elevation of intracellular Ca^{2+} triggers MBP phase transition

Weil et al., 2016, Cell Reports *16*, 314–322
July 12, 2016 © 2016 The Author(s).
http://dx.doi.org/10.1016/j.celrep.2016.06.008

CellPress

OPEN ACCESS
CellPress

Cell Reports
Report

Loss of Myelin Basic Protein Function Triggers Myelin Breakdown in Models of Demyelinating Diseases

Marie-Theres Weil,[1] Wiebke Möbius,[3,4] Anne Winkler,[5] Torben Ruhwedel,[3,4] Claudia Wrzos,[5] Elisa Romanelli,[6] Jeffrey L. Bennett,[7] Lukas Enz,[8] Norbert Goebels,[9] Klaus-Armin Nave,[3,4] Martin Kerschensteiner,[6,11] Nicole Schaeren-Wiemers,[8] Christine Stadelmann,[5] and Mikael Simons[1,2,10,11,*]

[1]Max Planck Institute of Experimental Medicine, 37075 Göttingen, Germany
[2]Institute of Neuronal Cell Biology, Technical University Munich, 80805 Munich, Germany
[3]Department of Neurogenetics, Max Planck Institute of Experimental Medicine, 37075 Göttingen, Germany
[4]Center Nanoscale Microscopy and Molecular Physiology of the Brain (CNMPB), 37075 Göttingen, Germany
[5]Department of Neuropathology, University of Göttingen Medical Center, 37075 Göttingen, Germany
[6]Institute of Clinical Neuroimmunology and Biomedical Center, Ludwig-Maximillians University, 80539 Munich, Germany
[7]Departments of Neurology, University of Denver, Denver, CO 80045, USA
[8]Neurobiology, Department of Biomedicine, University Hospital Basel, University of Basel, 4031 Basel, Switzerland
[9]Department of Neurology, Medical Faculty, Heinrich-Heine-University, 40225 Düsseldorf, Germany
[10]German Center for Neurodegenerative Disease (DZNE), 6250 Munich, Germany
[11]Munich Cluster for Systems Neurology (SyNergy), 81377 Munich, Germany
*Correspondence: msimons@gwdg.de
http://dx.doi.org/10.1016/j.celrep.2016.06.008

SUMMARY

Breakdown of myelin sheaths is a pathological hallmark of several autoimmune diseases of the nervous system. We employed autoantibody-mediated animal models of demyelinating diseases, including a rat model of neuromyelitis optica (NMO), to target myelin and found that myelin lamellae are broken down into vesicular structures at the innermost region of the myelin sheath. We demonstrated that myelin basic proteins (MBP), which form a polymer in between the myelin membrane layers, are targeted in these models. Elevation of intracellular Ca^{2+} levels resulted in MBP network disassembly and myelin vesiculation. We propose that the aberrant phase transition of MBP molecules from their cohesive to soluble and non-adhesive state is a mechanism triggering myelin breakdown in NMO and possibly in other demyelinating diseases.

INTRODUCTION

Myelin is the target of several autoimmune diseases, among which multiple sclerosis (MS) is the most common (Popescu and Lucchinetti, 2012). The primary target of the autoimmune attack in MS is not known but thought to be localized on the surface of the myelin sheath, from where the damage may spread in a retrograde fashion to the oligodendrocyte cell body (“outside in”). In addition, “inside-out” models of myelin damage in MS have been suggested (Henderson et al., 2009; Traka et al., 2016).

In neuromyelitis optica (NMO), another demyelinating disease, humoral immune reaction against aquaporin-4 (AQP4) on astrocytic endfeet (Jarius et al., 2008; Lennon et al., 2005) induces secondary oligodendrocyte cell death followed by myelin loss (Wrzos et al., 2014). The damage in NMO is believed to spread from the cell body to the myelin sheath in an inside-out fashion. Although the primary autoimmune effectors are different, the final result is, in both cases, the rapid breakdown of myelin sheaths. The purpose of this study was twofold: to determine the patterns of myelin fragmentation in different models of myelin diseases, and to understand the molecular basis of myelin degeneration.

Since myelin basic protein (MBP) is the only structural myelin protein known to be absolutely required for generating compact myelin sheaths, we hypothesized that it is also the key to our understanding of myelin degeneration. One defining feature of MBP is its intrinsically disordered polypeptide chain with a strong basic character (Musse et al., 2008). When MBP binds to two opposing negatively charged cytoplasmic leaflets of the myelin membrane, the positive charge in MBP is neutralized, and self-assembly into a polymeric network is induced. This process resembles a phase transition as it converts the soluble and freely dispersed MBP molecules into a liquid-like condensed state, thereby bringing together the cytoplasmic surfaces of the myelin bilayer and generating the tightly compacted multilamellar membrane stacks (Aggarwal et al., 2013). Phase transitions of proteins into condensed liquid states are emerging as a universal process underlying cellular organization (Hyman et al., 2014; Weber and Brangwynne, 2012). A challenge confronting this field is to connect in vitro protein phase behavior with in vivo processes. Here, we use models of demyelinating diseases to target the myelin sheath directly or indirectly and combined morphological and molecular analyses to

This is an open access article under the CC BY-NC-ND license (http://creativecommons.org/licenses/by-nc-nd/4.0/).

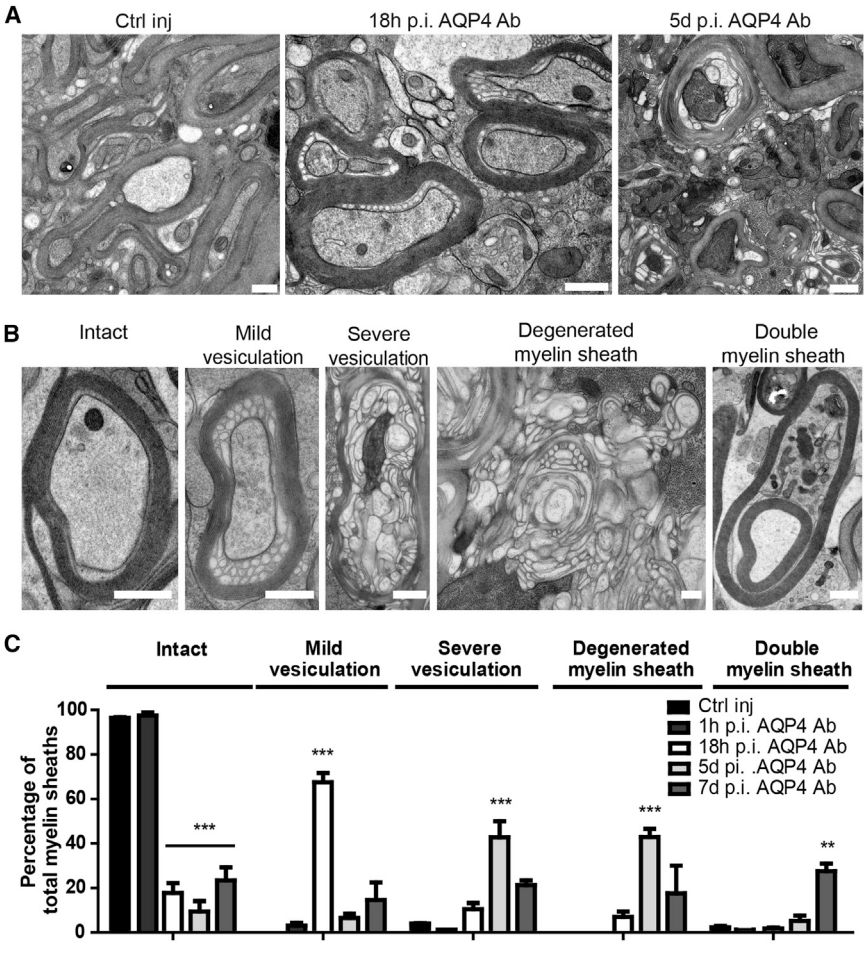

Figure 1. Myelin Pathology in Focal Experimental NMO Lesions Starts with Vesiculation of Myelin at the Inner Tongue

(A) Representative images of cross-sections of corpus callosum of Lewis rats injected with human AQP4 antibody (Ab) and complement or PBS (Ctrl) at indicated time points (scale bar, 500 nm).

(B) Myelin fragmentation profiles with representative images.

(C) Quantification of the myelin breakdown patterns at the different time points post-injection (1 hr, 18 hr, 5 days, and 7 days post-injection [p.i.]). Bars represent mean with SEM (n = 3 animals, >300 axons per animal; $^{**}p < 0.01$, $^{***}p < 0.001$, one-way ANOVA).

See also Figures S1 and S2.

demonstrate that the vesicular disruption of the myelin sheath is a common feature of myelin degeneration induced by the depolymerization of MBP molecules.

RESULTS

Vesicular Myelin Degeneration in a Focal NMO Model

We and others have previously established a focal NMO model (Saadoun et al., 2010; Wrzos et al., 2014), in which a human NMO recombinant antibody (AQP4 Ab) (Bennett et al., 2009) is stereotactically injected together with complement into the brain of Lewis rats. A few hours after the injection, astrocyte cell death is triggered, followed by loss of oligodendrocytes and secondary demyelination. The pathology depends on the AQP4 antibody, as complement alone (Figure S1A) or a control human antibody with complement fails to induce lesions (Wrzos et al., 2014). To characterize the ultrastructural features of myelin degeneration, we injected 1 μl AQP4 Ab (2.5 μg/μl) with complement (15 U/ml) or 1 μl PBS into the corpus callosum of Lewis rats and prepared tissue sections 1 and 18 hr, as well as 5 and 7 days post-injection. To prevent fixation artifacts that frequently occur in myelin in chemically fixed and dehydrated tissue (Möbius et al., 2010), we performed electron microscopy (EM) on high-pressure frozen tissue from focal NMO lesions. Since this method allows the visualization of myelin ultrastructure close to its native state, it enabled us to detect early myelin degeneration profiles. At 1 hr post-injection, myelin appeared intact and was indistinguishable from control lesions. However, when NMO lesions were analyzed 18 hr post-injection, ~80% of myelin sheaths showed pathological features (Figure 1A–1C). Strikingly, most of the fragmented myelin displayed vesiculated membrane profiles at the innermost layers of the sheath. At 18 hr post-injection, this fragmentation pattern was observed in nearly ~70% of the sheaths. At 5 days post-injection, the fraction of myelin with vesiculated sheaths at the innermost layers decreased, whereas sheaths with more advanced vesiculation patterns, with only a few compact layers remaining, increased. Furthermore, fully degenerated and vesiculated myelin sheaths that were often not associated with axons any longer were seen more frequently at 5 and 7 days post-injection. Thus, in the focal NMO model, myelin breakdown appears to start at the inner layers and progresses outward with time.

Fragmentation of the Myelin Sheath by Anti-MOG Antibodies

In addition to AQP4 antibodies, anti-MOG antibodies have been detected in a subgroup of patients with NMO, but also in childhood acute disseminated encephalomyelitis (Ikeda et al., 2015; Pröbstel et al., 2011; Sato et al., 2014). Whereas antibodies against AQP4 damage myelin via injury of astrocytes (Wrzos et al., 2014), the binding of anti-MOG antibodies occurs directly onto the surface of myelin sheaths. To analyze whether such a direct attack on myelin sheaths induces distinct fragmentation patterns, we performed stereotactic injections with a humanized anti-MOG antibody (8-18C5) (Kuenzle et al., 2007; Linington et al., 1988) and complement into the corpus callosum of Lewis rats. As expected, anti-MOG antibodies induced a more rapid fragmentation of myelin than anti-AQP4 antibodies (Figures 2A–2C). Since these lesions were almost entirely demyelinated

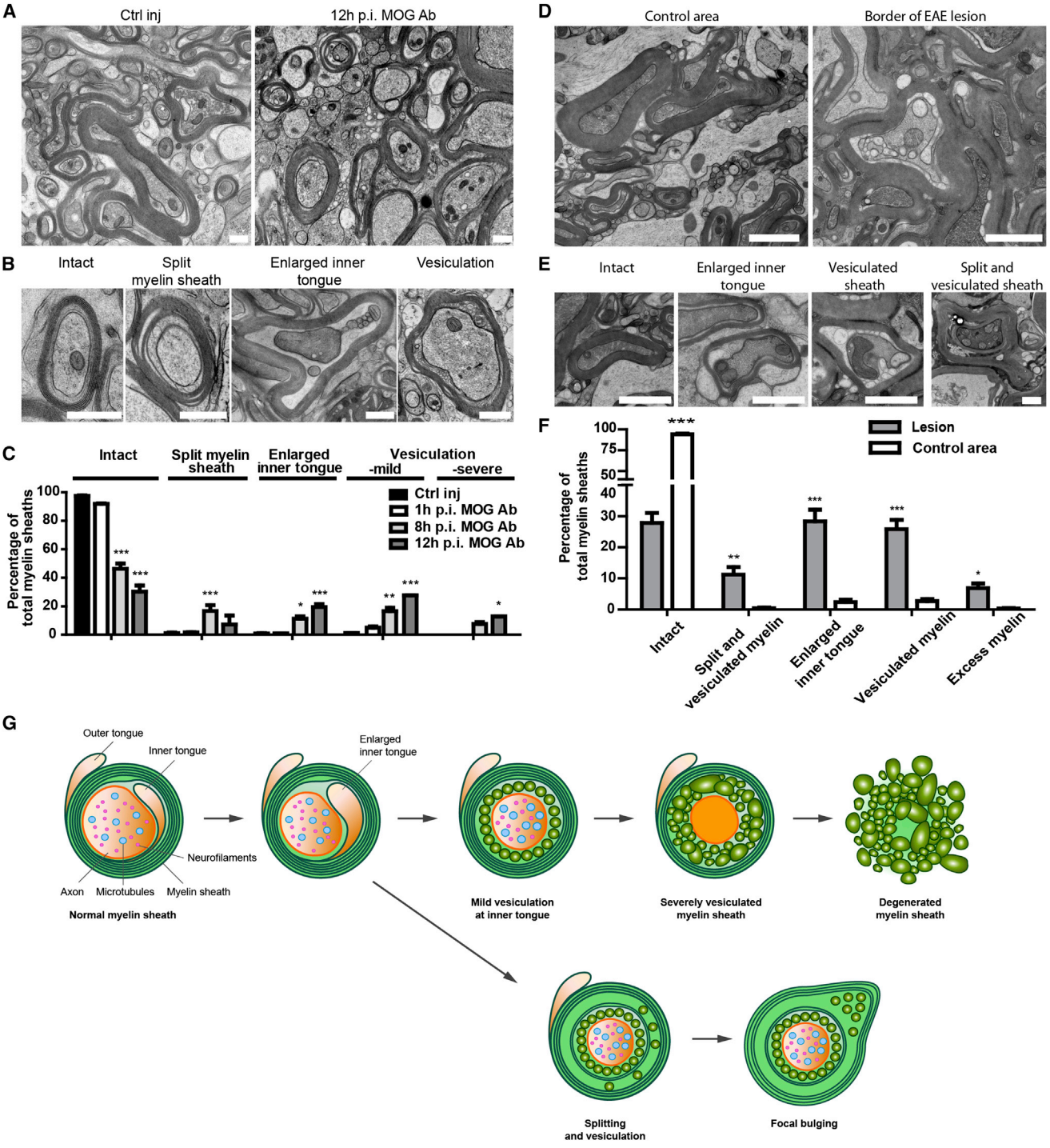

Figure 2. Myelin Fragmentation Patterns in Anti-MOG Antibody-Injected Lewis Rats and Biozzi EAE

(A) Representative images of cross-sections of MOG antibody (Ab) and complement (right) or PBS (Ctrl) injections (left) into the corpus callosum of adult Lewis rats at 12 hr p.i. Scale bar in all images, 500 nm.

(B) Pattern of myelin breakdown detected after focal injection of MOG antibody and complement.

(C) Quantification of the different myelin fragmentation profiles depicted in (B) as percentage of total myelin sheaths at 1 hr, 8 hr or 12 hr p.i. of MOG antibody/complement or PBS (Ctrl).

(D) Representative images of cross-sections of Biozzi EAE spinal cord lesions (first relapse). The left panel displays control area, whereas the right panel displays border of demyelinated EAE lesion.

(E) Myelin breakdown profiles detected in EAE lesions.

(legend continued on next page)

at 15 hr post-injection, we used earlier time points to detect patterns of myelin fragmentation. At 8 hr post-injection, approximately half of the myelin sheaths showed signs of injury. Compared to lesions induced by anti-AQP4 antibodies, the fragmentation patterns induced by anti-MOG antibodies were more heterogeneous. We observed myelin sheaths with split lamellae, enlarged inner tongue, and vesicular disruption. Approximately 20% of the myelin sheaths were vesiculated at the innermost layers of the myelin sheath. We also found a relatively high fraction of myelin sheaths with focal splitting of the myelin lamellae. In contrast to focal NMO using anti-AQP4 antibodies, there were hardly any fully disrupted and vesiculated myelin sheaths visible at any of the time points.

To analyze whether vesicular degeneration is also a feature of experimental autoimmune encephalomyelitis (EAE), we induced EAE in Biozzi mice, as these mice are characterized by a demyelinating antibody response following immunization with MOG protein. The spinal cord of the diseased mice was dissected, lesions were localized macroscopically, and samples were processed by high-pressure freezing. The lesion-containing samples were analyzed at the borders of the lesions that were actively demyelinating. Similar to the focal anti-MOG/complement injections, two major patterns of myelin fragmentation were observed. We found both sheaths with signs of vesicular disruption of the adaxonal region of the myelin sheath as well as sheaths with focal splitting that in some cases resulted in the formation of myelin outfoldings (Figures 2D–2F).

We also analyzed patterns of myelin breakdown in the cuprizone mouse model of demyelination. Myelin vesiculation at the innermost membranes was observed in nearly ~40% of the sheaths after 3 weeks of cuprizone feeding (Figure S2). Thus, the vesicular transformation of the innermost layers of myelin appears to be a common feature of myelin breakdown. However, whereas this pattern represents the major form of myelin fragmentation in focal NMO, anti-MOG antibody-mediated myelin damage results, additionally, in splitting and loosening of myelin layers (Figure 2G).

Loss of MBP Triggers Vesicular Disruption of Myelin

Since MBP is the only protein known to be required for myelin assembly, we hypothesized that loss of MBP function may trigger myelin disassembly. We performed cryo-immunoelectron microscopy on experimental focal NMO lesions to determine the localization of MBP in the disrupted myelin sheaths. Strikingly, we found that MBP was almost undetectable in the adaxonal space of the myelin sheath containing the vesiculated and fragmented membrane profiles but was readily stained in the still compacted layers. To exclude poor antibody penetration as an underlying cause, we stained sections with antibodies against PLP, another constituent of compacted myelin. We found robust staining of PLP in both the compacted and the vesiculated areas of myelin. Thus, MBP appears to be displaced from the inner vesiculated membrane profiles of degenerating myelin, raising the possibility that a release of MBP from the inner leaflet of the membrane bilayer triggers myelin vesiculation (Figures 3A and 3B).

To determine whether loss of MBP triggers myelin fragmentation, we studied high-pressure frozen optic nerves of *shiverer* mice that lack MBP at postnatal day 10 (P10), P14, and P21 (Figures 3C–3E). As noted previously (Popko et al., 1987; Snaidero et al., 2014), our high-resolution EM analyses of *shiverer* mice showed that the majority of myelin sheaths have only up to four layers of uncompacted wraps and a fraction of sheaths displayed vesicular membrane profiles. Interestingly, the fraction of myelin sheaths with vesiculated membrane profiles increased dramatically at P21 (~80% of the myelin sheaths), demonstrating that MBP is required to maintain the physical stability of the sheaths.

Epitope Unmasking in MBP during Myelin Fragmentation

MBP can switch between two different functional states (Aggarwal et al., 2013). There is a soluble phase, in which MBP molecules are freely dispersed in the cytoplasm with very little secondary structure and rarely interacting with each other; and a condensed phase, in which MBP molecules are concentrated into a network at the interphase of two cytoplasmic membrane surfaces. Thus, we hypothesized that such a transition may be the underlying cause of myelin vesiculation. To recognize the two different functional states of MBP molecules, we first needed to design tools that allow their discrimination. We hypothesized that domains that are engaged in molecular interactions of MBP become unmasked, when MBP molecules are depolymerized and converted into their dispersed phase.

We have previously shown that hydrophobic phenylalanine residues are required for the polymerization of MBP (Aggarwal et al., 2013). Since MBP network assembly requires molecular interactions mediated by phenylalanine residues, their exposure in myelin could be used as a measure of network disassembly. Previously, an antibody (QD9) against human MBP residues 82–88 was shown to specifically stain areas of degenerated myelin (Matsuo et al., 1997, 1998). Interestingly, this epitope is localized adjacent to one of the double phenylalanine motifs (F4,5 in the amphipathic helix amino acids 85–92) raising the possibility that this antibody only recognizes the MBP molecules, when converted into their dispersed and dysfunctional state.

First, we confirmed by western blotting that QD9 recognizes full-length monomeric and not a proteolytic fragment of MBP (Figure S1B). In addition, we found that QD9 immuno-stained

(F) Quantification of percentage of all different fragmentation patterns in EAE lesion and control area. Bars display mean with SEM (n = 3 animals, >300 axons per animal; *p < 0.05, **p < 0.01, ***p < 0,001, one-way ANOVA).

(G) Schematic drawing of proposed model of myelin fragmentation. A normal myelin sheath with its compacted layers (in green) wrapped around an axon (with microtubules in blue and neurofilaments in pink) is depicted. The cytoplasm-rich domains of myelin at the outer and inner tongue are shown in orange. In the focal NMO model, first the inner tongue becomes enlarged before it collapses into small vesicles at the inside of the myelin sheath. The vesiculation progresses outward until the whole myelin sheath is transformed into vesicular profiles. The lower panel shows additional patterns observed in the anti-MOG antibody model consisting of focal splitting and vesiculations with focal bulging.

See also Figures S1 and S2.

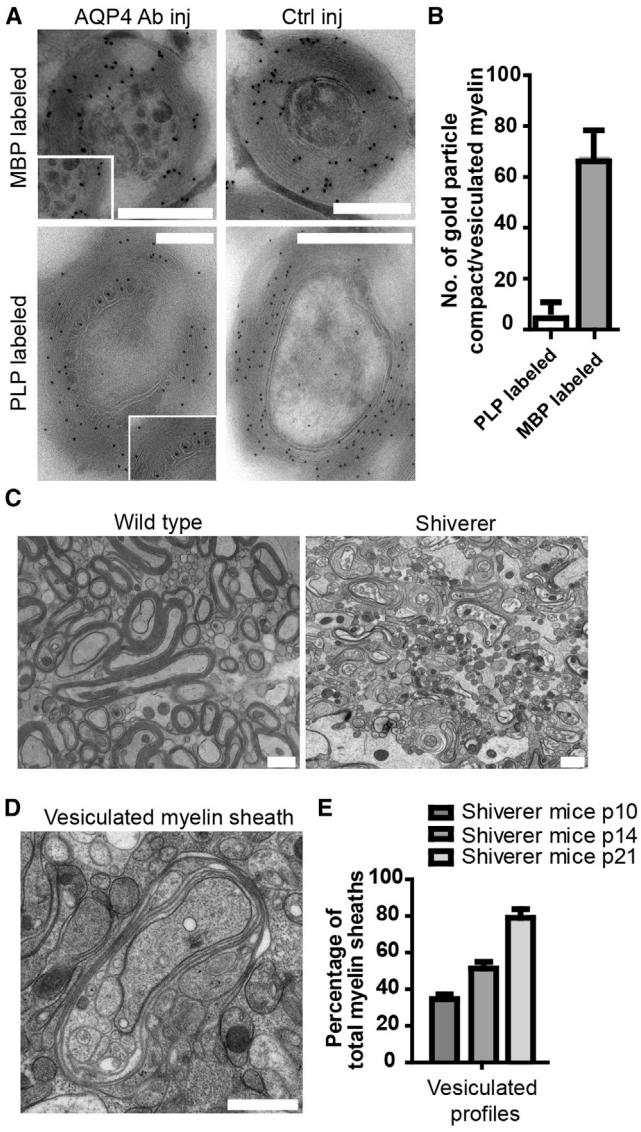

Figure 3. Lack of MBP Leads to Myelin Vesiculation

(A) Adult Lewis rats were injected with human AQP4 antibody (Ab) and complement or PBS (Ctrl) in the corpus callosum. The subcellular localization of MBP (top) and PLP (bottom) was determined by cryoimmuno-electron microscopy at 18 hr p.i. (scale bar, 500 nm; gold size, 15 nm for MBP and 10 nm for PLP). The vesicles at the inner tongue are enlarged in the white boxes.

(B) Quantification of the number of gold particles in compact myelin as compared to gold particles in vesiculated myelin for MBP and PLP labeling. Bars shown mean with SEM (n = 3 animals, >70 axons per animal; ***$p < 0.001$, Student's t test).

(C and D) Representative images of high-pressure frozen optic nerves of wild-type and *shiverer* mice at P10, P14, and P21 (C) with magnification of a vesiculated sheath in (D).

(E) Quantification of vesiculated membrane profiles. Bars shown mean with SEM (n = 3 animals, >80 axons per animal; ***$p < 0.001$, Student's t test).

See also Figure S1.

MBP when expressed in fibroblast or epithelial cell lines (Figure S2C). However, when primary cultures of oligodendrocytes were stained with QD9, we observed very little labeling of MBP (Figure S3), which is in contrast to the robust MBP staining when using a polyclonal antibody against MBP (total MBP, subsequently only termed MBP). Next, we treated primary cultures of oligodendrocytes with ionomycin and sphingosine to antagonize the electrostatic interactions of MBP with lipids and to release it from its membrane-bound state (Figure S3). We observed rapid unmasking of the QD9 epitope, and quantification of the integrated intensity revealed a dramatic increase in the MBP/QD9 ratio. These results suggest that QD9 only detects MBP when present in a non-physiological state.

This was further highlighted in cryosections of chronic active MS lesions, in which we observed QD9 antibody staining at lesion borders within areas containing CD68-positive macrophages (Figure S4). However, chronic inactive lesions did not show any staining at all, and normal appearing white and gray matter showed sporadically QD9-positive fibers as in control cases. These data demonstrate that the QD9 antibody does not stain all myelinated fibers, but only fibers in areas, where myelin damage might be ongoing.

Calcium Switches the Functional States of MBP Molecules in NMO

Since MBP is known to interact with phosphatidylinositol 4,5-bisphosphate (PIP2) (Musse et al., 2008; Nawaz et al., 2009), we tested whether increasing intracellular Ca^{2+} levels using ionomycin loosens binding of MBP to PIP2. Indeed, we observed that staining intensity of PIP2 increases in oligodendrocytes after treatment with ionomycin (Figure S3). Thus, by increasing intracellular Ca^{2+} levels in oligodendrocytes, the binding of MBP to the cytoplasmic leaflet of the membrane bilayer weakens, and the QD9 epitope becomes exposed.

To determine whether a rise in intracellular Ca^{2+} levels can also displace MBP from myelin, we treated acute brain slices with ionomycin. Ionomycin was added to the slices and QD9 and MBP staining intensity determined 5, 15, and 30 min after the treatment. As observed in cell culture, we detected a marked increase in the ratio of MBP/QD9 staining intensity after Ca^{2+} elevation in the area of the corpus callosum (Figure S3). As shown previously in conventionally fixed samples (Schlaepfer, 1977), EM of high-pressure frozen samples revealed a pattern of myelin fragmentation (Figure S3) that was indistinguishable from NMO lesions consisting of myelin sheaths with vesicular fragmentation profiles at the innermost layers of the myelin sheath.

Next, we determined the QD9 and MBP staining intensity in the focal NMO model. When animals were analyzed 18 hr after the injection, we observed a marked increase in the MBP/QD9 staining ratio in the focal NMO lesions (Figures 4A–4C). At this time point, MBP staining intensity was similar in focal NMO and control lesions, indicating that myelin sheaths were not yet cleared away (Wrzos et al., 2014).

Since our results indicated that elevated intracellular Ca^{2+} levels are able to disassemble MBP molecular networks, we asked whether this also occurs in focal NMO lesions.

We injected 1 μl AQP4 antibody with complement or 1 μl PBS with complement into the corpus callosum of Lewis rats and prepared acute slice cultures 12 hr after injection, at a time point when astrocyte cell death had already occurred (Figures 4E and 4F). To chelate Ca^{2+} ions, slice cultures were subsequently

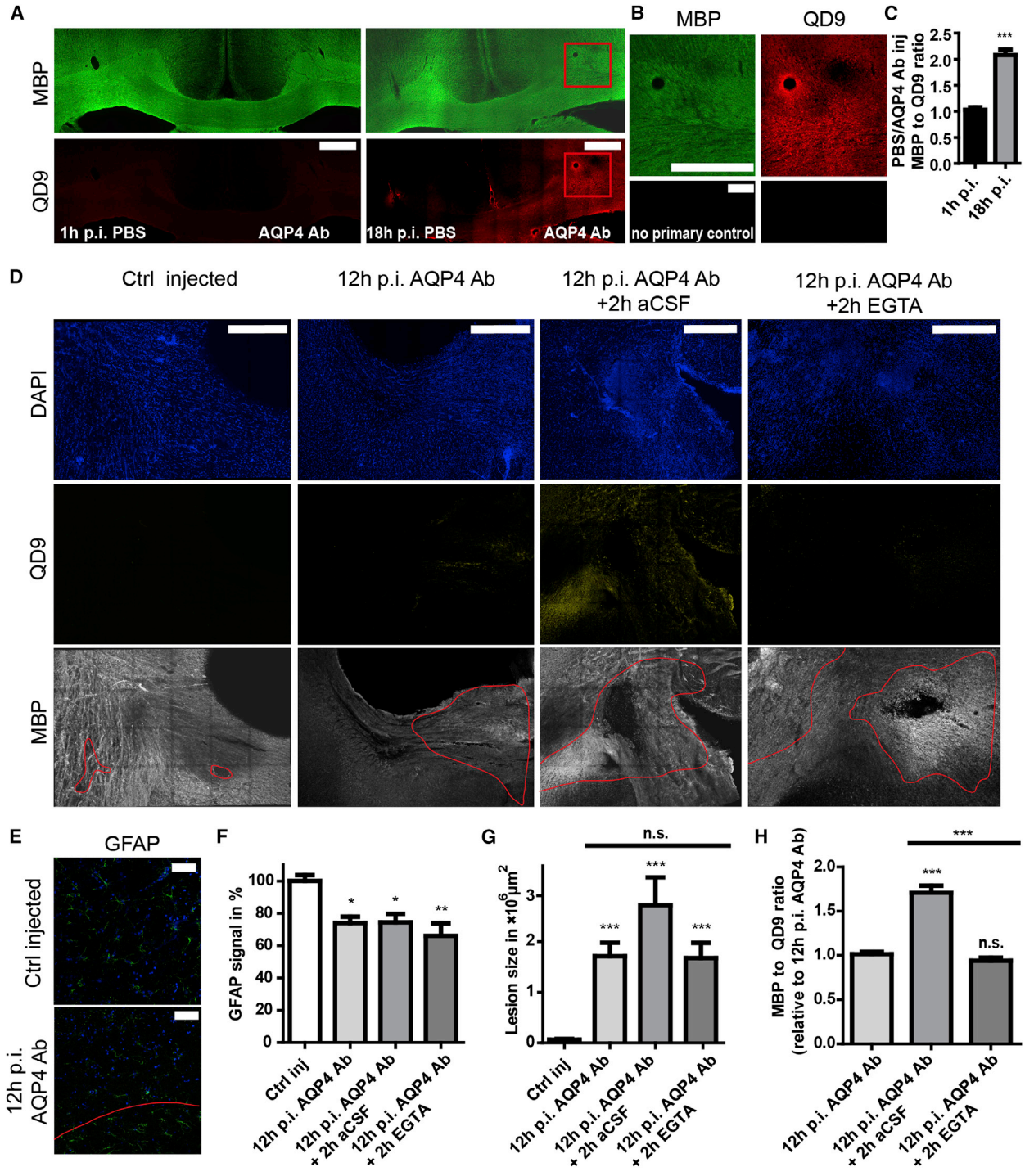

Figure 4. Calcium Influx Triggers Epitope Unmasking in MBP in Early NMO Lesions

(A) Representative images of coronal sections of adult Lewis rat brains injected with human AQP4 antibody (Ab) and complement or PBS (Ctrl) in the contralateral hemisphere for 1 hr or 18 hr p.i. stained for MBP in green and QD9 in red.

(B) Magnification of the red box in (A) and no primary antibody control to indicate that there is no cross-reactivity with the antibody injected. Scale bar, 1 mm (A and B).

(C) Quantification of the MBP to QD9 signal intensity ratio of the AQP4 antibody lesion normalized to the control (PBS injection) (n = 3 animals, 3–5 regions of same size per animal, ***$p < 0.001$, Student's t-test).

(D) Adult Lewis rat brains were injected with 1 µl human AQP4 antibody or PBS and complement. After 12 hr p.i., the rats were sacrificed, and acute brain slices were maintained for 2 hr in aCSF or aCSF supplemented with 25 mM EGTA. Sections were stained with DAPI in blue (upper panel), QD9 in yellow (middle panel), and MBP in grey (lower panel). Scale bar, 1 mm. The lesion area marked by the red line was determined by GFAP staining.

(legend continued on next page)

treated for 2 hr with EGTA, followed by staining with QD9 and MBP antibodies. Notably, chelating Ca^{2+} ions was able to bring down the ratio of MBP/QD9 staining intensity to control levels (Figures 4D, 4G, and 4H), suggesting that elevated intracellular Ca^{2+} levels are implicated in switching between the functional states of MBP molecules in focal NMO.

DISCUSSION

Here, we took advantage of recent advances in high-pressure freezing and freeze-substitution to improve tissue preservation and to elucidate myelin pathology close to its native state. Using different models of antibody-mediated demyelinating diseases, we find that myelin lamellae are broken down into vesicular structures at the innermost region of the myelin sheath. This pattern was most pronounced in the focal NMO model, but such fragmentation profiles were also observed in anti-MOG antibody-mediated lesions and the cuprizone model, suggesting that they represent a common pathological feature of degenerating myelin in diseases.

How does myelin break down in demyelinating diseases? We propose that MBP loses its interaction with the myelin membrane, which eventually, when the physical stabilization of myelin lamellae is compromised, appears to result in myelin vesiculation. Interestingly, this process appears to begin in the adaxonal region of myelin. Using EM of high-pressure frozen samples, the innermost tongue of the myelin sheath appears as a relatively large cytoplasm-rich compartment, which faces the periaxonal space along its entire length. This compartment is connected with small cytoplasm-rich channels that run through the myelin sheath and connect it with the cell body (Snaidero et al., 2014). Like a synapse, the innermost tongue of myelin might be particularly vulnerable to metabolic disturbances, possibly due to its high energy demand and its long distance from the cell body (Simons et al., 2014). Such a "dying-back" pathology from the inner tongue to the oligodendrocytes cell body has been observed previously in the cuprizone model (Ludwin and Johnson, 1981).

Another major pathological feature only observed after injecting anti-MOG antibody was the loosening and focal splitting of the myelin layers. Such a loosing of the myelin compaction might render myelin sheaths susceptible to the formation of myelin outfoldings that can be removed by phagocytes in MS models that combine a humoral anti-MOG response with cellular infiltration. These results concur with previous analyses of the initial stages of myelin destruction in MS lesions, where several patterns of myelin destruction were described, including vesicular degeneration of myelin (Périer and Grégoire, 1965; Raine et al., 1999; Genain et al., 1999; Stys, 2010). In addition, stripping of myelin from axons by the invasion of microglia/macrophages into the seemingly intact myelin sheath has also been observed (Yamasaki et al., 2014).

How does MBP lose its membrane association in degenerating myelin in NMO? We propose that a primary attack on the AQP4-rich astroglial endfeet spills over to oligodendrocytes by the release of unknown toxic mediators from astrocytes that raise intracellular oligodendroglial Ca^{2+}. Since the innermost tongue of the myelin sheath is connected via small cytoplasm-rich areas to the oligodendrocyte cell body, damage to the cell soma would lead to high intracellular Ca^{2+} and rapidly spread into the myelin sheaths. Such an increase in Ca^{2+} could affect the binding of MBP to the headgroups of PIP2 and phosphatidylserine in the lipid bilayer. Thus, the elevation of Ca^{2+} in myelin may trigger MBP network depolymerization and thereby induce rapid myelin vesiculation. Genetically encoded calcium sensors should be used in future studies to record the spatiotemporal pattern of calcium changes in myelin in models of NMO. In summary, we propose that MBP molecules function as a "switchable" glue and that the transition from the cohesive protein meshwork back into the single soluble components is key to the pathogenesis of myelin disorders.

EXPERIMENTAL PROCEDURES

All experiments were performed in accordance with the German animal welfare law and local regulations for animal experiments. The animals were kept in 12h light dark-cycles and bred in the animal facility of the Max Planck Institute of Experimental Medicine and the University Medical Center Göttingen.

Stereotactic Injection of Lewis Rats

Stereotactic injection of anti-MOG (8-18C5) or anti-AQP4 antibody (rAB-53) was carried out in adult Lewis rats obtained from Harlan. The rats were anaesthetized using an intraperitoneal (i.p.) injection of ketamine/xylazine and mounted in a stereotactic device. After drilling a fine hole through the skull 1 mm caudal to the bregma and 2 mm lateral to the sagittal suture, the glass capillary was inserted 3 mm deep to target the corpus callosum. The rats were then injected with 1 μl of antibody solution (2.5 μg/μl) with complement (15 U/ml) (Sigma-Aldrich) over a 5-min period. As a control, 1 μl of PBS was injected in the ipsilateral site of the brain. Monastral blue (Sigma-Aldrich) was added for lesion identification. After injection, the glass capillary was carefully withdrawn, and the injection site was sealed by suture.

Electron Microscopy

Animals used for EM studies were terminated by cervical dislocation, and the brain was removed quickly. The brain was then cut into 200 μm sections with the help of the Leica vibratome VT1200S. From these sections, the region of interest was cryofixed in 20% poly(vinyl-pyrrolidinone) (Sigma-Aldrich) using the high-pressure freezer Leica HPM100 (Leica). The tissue was then freeze-substituted using the Leica AFS II as described previously (Möbius et al., 2010; Snaidero et al., 2014) and Epon embedded. The Epon-embedded tissue was cut with the Leica Ultracut S ultramicrotome into 0.5-μm semithin sections or in ultrathin sections of 50 nm thickness that were contrasted with 4% uranylacetate (SPI-Chem) (Möbius et al., 2010). Electron micrographs were obtained using the electron microscopes Zeiss EM900 or LEO EM912AB (Zeiss)

(E) Representative images of a GFAP staining (in green) in control and AQP4 Ab injected rats. The loss of staining or astrocyte fragmentation is marked by the red line. Scale bar, 200 μm.
(F) Quantification of GFAP signal intensity around the injection site and lesion size.
(G) Quantification of lesion area based on GFAP loss in (E).
(H) Quantification of MBP to QD9 integrated density ratio as normalized to the 12 hr p.i. time point for control and EGTA treated acute brain sections. Graphs show the mean with SEM (n = 3 animals, *p < 0.05, **p < 0.01, ***p < 0.001, one-way ANOVA).
See also Figures S1, S3, and S4.

equipped with a wide-angle dual speed 2k-CCD-camera or on-axis 2k CCD-camera, respectively (TRS) using ImageSP or ITEM (Olympus) software. For quantification, at least 300 myelin sheaths that were cross-sectioned completely without artifacts and could be classified without doubt were counted. The myelin sheath was scored in one of the following categories: intact, split (more than half of the axon diameter), with enlarged inner tongue, vesiculated, or degenerated. The percentage of the fragmentation profile was calculated.

A full description of the experimental procedures used in this study can be found in in Supplemental Experimental Procedures.

SUPPLEMENTAL INFORMATION

Supplemental Information includes Supplemental Experimental Procedures and four figures and can be found with this article online at http://dx.doi.org/10.1016/j.celrep.2016.06.008.

AUTHOR CONTRIBUTIONS

M.-T.W. designed and performed experiments, analyzed the data, and wrote the manuscript. W.M., T.R., and K.-A.N. assisted with the EM experiments and data analysis. A.W. and C.W. performed experiments and analyzed the data. E.R. and M.K. performed the EAE experiments. L.E. and N. S.-W. performed and analyzed the immunohistochemistry on MS tissue. J.L.B. and N.G. provided the engineered humanized antibodies. C.S. and M.S. designed experiments, supervised research, and wrote the manuscript.

ACKNOWLEDGMENTS

We thank Boguslawa Sadowski for technical assistance in cutting sections for cryo-immunoelectron microscopy and Katja Schulz for help with immunohistochemistry. The work was supported by an ERC CoG Grant (to M.S.) and grants from the German Research Foundation (SI 746/9-1,10-1,11-1; TRR43), the Tschira-Stiftung, an ERC Advanced Investigator Grant AXOGLIA (to K.-A.N. and W.M.), the Cluster of Excellence and DFG Research Center for Nanoscale Microscopy and Molecular Physiology of the Brain (to W.M.), and SyNergy (to M.S.). Human work (N.S.-W. and L.E.) was supported by the Swiss National Science Foundation (grant 31003A-125210) and the Swiss Multiple Sclerosis Society. C.S. and M.S. were supported by grants from the Hertie Foundation and the Myelin Repair Foundation. J.L.B. was supported by grants from the NIH (EY022936), Guthy-Jackson Charitable Foundation, and a National MS Society Collaborative Research Center Grant.

Received: February 8, 2016
Revised: April 22, 2016
Accepted: May 26, 2016
Published: June 23, 2016

REFERENCES

Aggarwal, S., Snaidero, N., Pähler, G., Frey, S., Sánchez, P., Zweckstetter, M., Janshoff, A., Schneider, A., Weil, M.-T., Schaap, I.A.T., et al. (2013). Myelin membrane assembly is driven by a phase transition of myelin basic proteins into a cohesive protein meshwork. PLoS Biol. *11*, e1001577.

Bennett, J.L., Lam, C., Kalluri, S.R., Saikali, P., Bautista, K., Dupree, C., Glogowska, M., Case, D., Antel, J.P., Owens, G.P., et al. (2009). Intrathecal pathogenic anti-aquaporin-4 antibodies in early neuromyelitis optica. Ann. Neurol. *66*, 617–629.

Genain, C.P., Cannella, B., Hauser, S.L., and Raine, C.S. (1999). Identification of autoantibodies associated with myelin damage in multiple sclerosis. Nat. Med. *5*, 170–175.

Henderson, A.P.D., Barnett, M.H., Parratt, J.D.E., and Prineas, J.W. (2009). Multiple sclerosis: distribution of inflammatory cells in newly forming lesions. Ann. Neurol. *66*, 739–753.

Hyman, A.A., Weber, C.A., and Jülicher, F. (2014). Liquid-liquid phase separation in biology. Annu. Rev. Cell Dev. Biol. *30*, 39–58.

Ikeda, K., Kiyota, N., Kuroda, H., Sato, D.K., Nishiyama, S., Takahashi, T., Misu, T., Nakashima, I., Fujihara, K., and Aoki, M. (2015). Severe demyelination but no astrocytopathy in clinically definite neuromyelitis optica with anti-myelin-oligodendrocyte glycoprotein antibody. Mult. Scler. *21*, 656–659.

Jarius, S., Aboul-Enein, F., Waters, P., Kuenz, B., Hauser, A., Berger, T., Lang, W., Reindl, M., Vincent, A., and Kristoferitsch, W. (2008). Antibody to aquaporin-4 in the long-term course of neuromyelitis optica. Brain *131*, 3072–3080.

Kuenzle, S., von Büdingen, H.-C., Meier, M., Harrer, M.D., Urich, E., Becher, B., and Goebels, N. (2007). Pathogen specificity and autoimmunity are distinct features of antigen-driven immune responses in neuroborreliosis. Infect. Immun. *75*, 3842–3847.

Lennon, V.A., Kryzer, T.J., Pittock, S.J., Verkman, A.S., and Hinson, S.R. (2005). IgG marker of optic-spinal multiple sclerosis binds to the aquaporin-4 water channel. J. Exp. Med. *202*, 473–477.

Linington, C., Bradl, M., Lassmann, H., Brunner, C., and Vass, K. (1988). Augmentation of demyelination in rat acute allergic encephalomyelitis by circulating mouse monoclonal antibodies directed against a myelin/oligodendrocyte glycoprotein. Am. J. Pathol. *130*, 443–454.

Ludwin, S.K., and Johnson, E.S. (1981). Evidence for a "dying-back" gliopathy in demyelinating disease. Ann. Neurol. *9*, 301–305.

Matsuo, A., Lee, G.C., Terai, K., Takami, K., Hickey, W.F., McGeer, E.G., and McGeer, P.L. (1997). Unmasking of an unusual myelin basic protein epitope during the process of myelin degeneration in humans: a potential mechanism for the generation of autoantigens. Am. J. Pathol. *150*, 1253–1266.

Matsuo, A., Akiguchi, I., Lee, G.C., McGeer, E.G., McGeer, P.L., and Kimura, J. (1998). Myelin degeneration in multiple system atrophy detected by unique antibodies. Am. J. Pathol. *153*, 735–744.

Möbius, W., Cooper, B., Kaufmann, W.A., Imig, C., Ruhwedel, T., Snaidero, N., Saab, A.S., and Varoqueaux, F. (2010). Electron microscopy of the mouse central nervous system. Methods Cell Biol. *96*, 475–512.

Musse, A.A., Gao, W., Homchaudhuri, L., Boggs, J.M., and Harauz, G. (2008). Myelin basic protein as a "PI(4,5)P2-modulin": a new biological function for a major central nervous system protein. Biochemistry *47*, 10372–10382.

Nawaz, S., Kippert, A., Saab, A.S., Werner, H.B., Lang, T., Nave, K.-A., and Simons, M. (2009). Phosphatidylinositol 4,5-bisphosphate-dependent interaction of myelin basic protein with the plasma membrane in oligodendroglial cells and its rapid perturbation by elevated calcium. J. Neurosci. *29*, 4794–4807.

Périer, O., and Grégoire, A. (1965). Electron microscopic features of multiple sclerosis lesions. Brain *88*, 937–952.

Popescu, B.F.G., and Lucchinetti, C.F. (2012). Pathology of demyelinating diseases. Annu. Rev. Pathol. *7*, 185–217.

Popko, B., Puckett, C., Lai, E., Shine, H.D., Readhead, C., Takahashi, N., Hunt, S.W., 3rd, Sidman, R.L., and Hood, L. (1987). Myelin deficient mice: expression of myelin basic protein and generation of mice with varying levels of myelin. Cell *48*, 713–721.

Pröbstel, A.K., Dornmair, K., Bittner, R., Sperl, P., Jenne, D., Magalhaes, S., Villalobos, A., Breithaupt, C., Weissert, R., Jacob, U., et al. (2011). Antibodies to MOG are transient in childhood acute disseminated encephalomyelitis. Neurology *77*, 580–588.

Raine, C.S., Cannella, B., Hauser, S.L., and Genain, C.P. (1999). Demyelination in primate autoimmune encephalomyelitis and acute multiple sclerosis lesions: a case for antigen-specific antibody mediation. Ann. Neurol. *46*, 144–160.

Saadoun, S., Waters, P., Bell, B.A., Vincent, A., Verkman, A.S., and Papadopoulos, M.C. (2010). Intra-cerebral injection of neuromyelitis optica immunoglobulin G and human complement produces neuromyelitis optica lesions in mice. Brain *133*, 349–361.

Sato, D.K., Callegaro, D., Lana-Peixoto, M.A., Waters, P.J., de Haidar Jorge, F.M., Takahashi, T., Nakashima, I., Apostolos-Pereira, S.L., Talim, N., Simm, R.F., et al. (2014). Distinction between MOG antibody-positive and AQP4 antibody-positive NMO spectrum disorders. Neurology *82*, 474–481.

Schlaepfer, W.W. (1977). Vesicular disruption of myelin simulated by exposure of nerve to calcium ionophore. Nature *265*, 734–736.

Simons, M., Misgeld, T., and Kerschensteiner, M. (2014). A unified cell biological perspective on axon-myelin injury. J. Cell Biol. *206*, 335–345.

Snaidero, N., Möbius, W., Czopka, T., Hekking, L.H.P., Mathisen, C., Verkleij, D., Goebbels, S., Edgar, J., Merkler, D., Lyons, D.A., et al. (2014). Myelin membrane wrapping of CNS axons by PI(3,4,5)P3-dependent polarized growth at the inner tongue. Cell *156*, 277–290.

Stys, P.K. (2010). Multiple sclerosis: autoimmune disease or autoimmune reaction? Can. J. Neurol. Sci. *37* (*Suppl 2*), S16–S23.

Traka, M., Podojil, J.R., McCarthy, D.P., Miller, S.D., and Popko, B. (2016). Oligodendrocyte death results in immune-mediated CNS demyelination. Nat. Neurosci. *19*, 65–74.

Weber, S.C., and Brangwynne, C.P. (2012). Getting RNA and protein in phase. Cell *149*, 1188–1191.

Wrzos, C., Winkler, A., Metz, I., Kayser, D.M., Thal, D.R., Wegner, C., Brück, W., Nessler, S., Bennett, J.L., and Stadelmann, C. (2014). Early loss of oligodendrocytes in human and experimental neuromyelitis optica lesions. Acta Neuropathol. *127*, 523–538.

Yamasaki, R., Lu, H., Butovsky, O., Ohno, N., Rietsch, A.M., Cialic, R., Wu, P.M., Doykan, C.E., Lin, J., Cotleur, A.C., et al. (2014). Differential roles of microglia and monocytes in the inflamed central nervous system. J. Exp. Med. *211*, 1533–1549.

Cell Reports, Volume *16*

Supplemental Information

Loss of Myelin Basic Protein Function Triggers Myelin Breakdown in Models of Demyelinating Diseases

Marie-Theres Weil, Wiebke Möbius, Anne Winkler, Torben Ruhwedel, Claudia Wrzos, Elisa Romanelli, Jeffrey L. Bennett, Lukas Enz, Norbert Goebels, Klaus-Armin Nave, Martin Kerschensteiner, Nicole Schaeren-Wiemers, Christine Stadelmann, and Mikael Simons

Supplemental Figures:

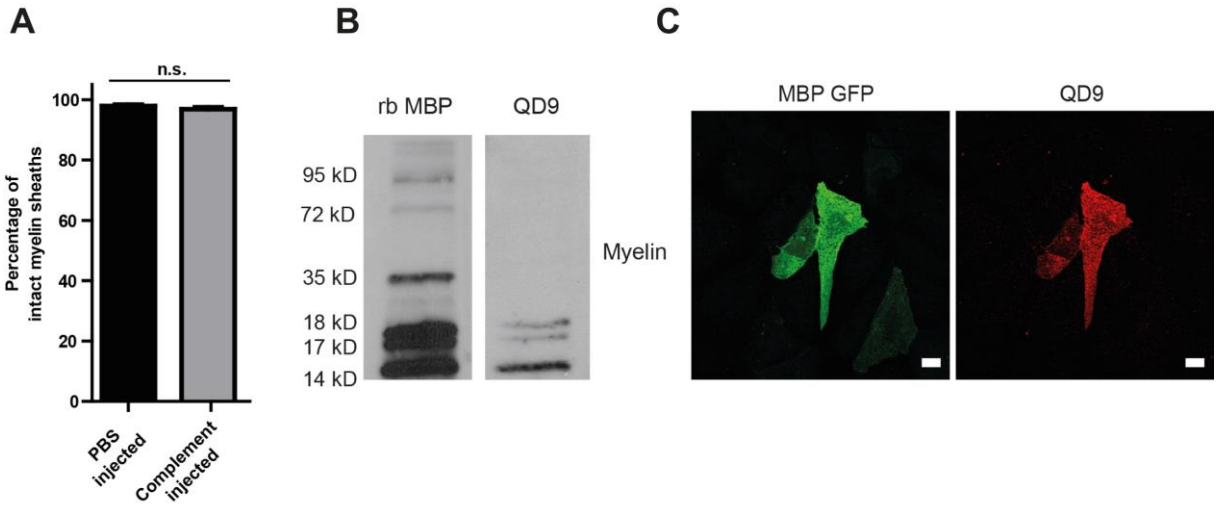

Figure S1. Complement injection does not cause myelin damage; and QD9 recognizes MBP, related to Figure 1, 2, 3 and 4 (A) Quantification of myelin fragmentation upon complement or PBS injection (18 h p.i.) in the corpus callosum of Lewis rats. Bars represent mean with SEM (n=3 animals, >250 axons per animal, Student's t-test). (B) QD9 detects full length monomeric MBP in Western blots of myelin preparations and MBP-GFP transfected PtK2 cells (C) (for all images: scale bar 25 µm).

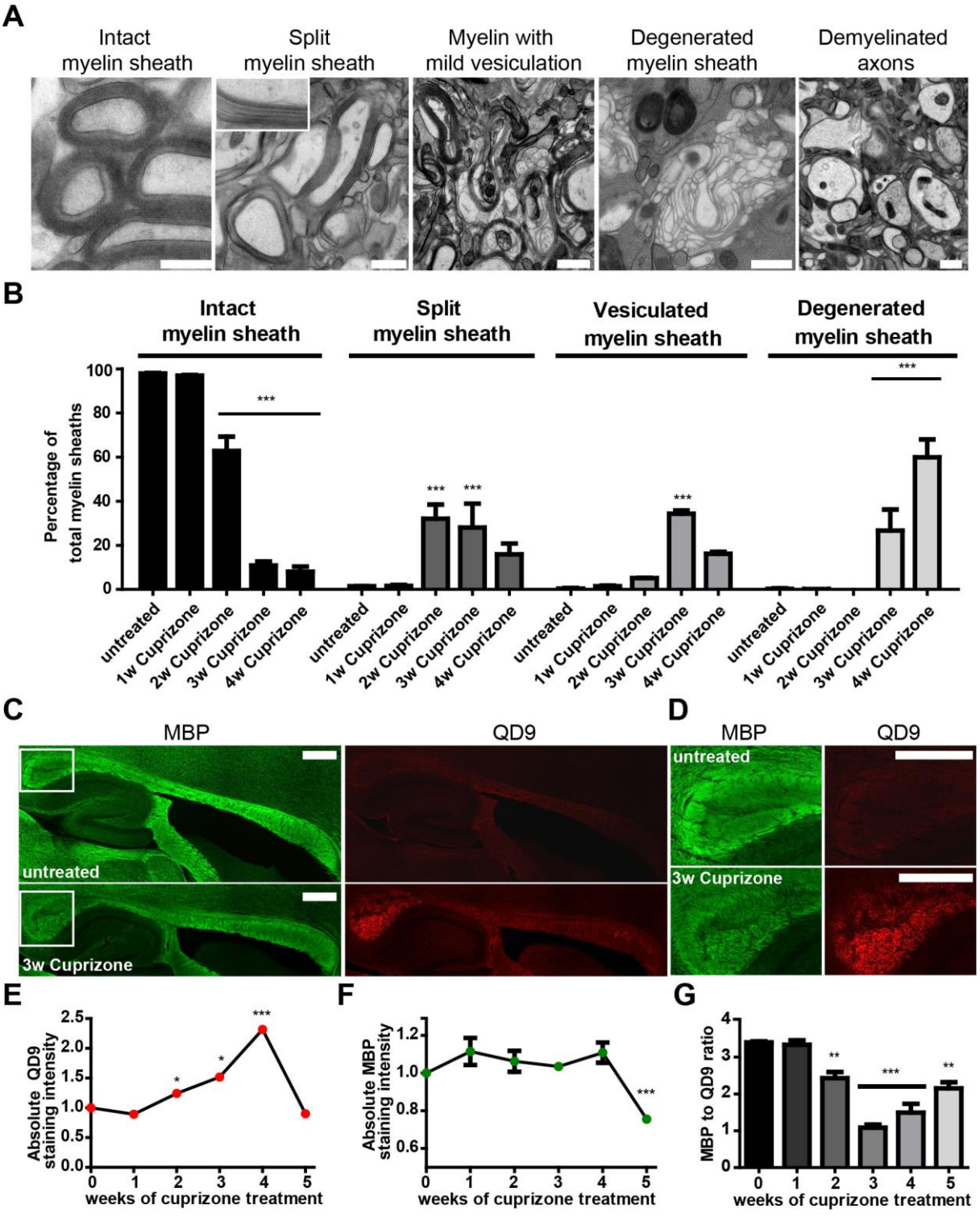

Figure S2. Myelin pathology in cuprizone fed mice starts with vesiculation of myelin at the inner tongue and induces unmasking of the QD9 epitope, related to Figure 1 and 2.
(A) Representative images of cross-sections of C57/B6N mice fed with 0.2 % cuprizone (scale bar 500 nm). The white box displays magnification of split myelin sheath at 2 weeks of cuprizone treatment. (B) Quantification of the percentage of different myelin fragmentation profiles during cuprizone treatment. Bars shown mean with SEM (n=3 animals, >300 axons per animal, **=p<0.01, ***=p<0.001, ANOVA). (C) Representative images of sagittal brain sections of C57/B6N mice fed with 0.2 % cuprizone (scale bar 1 mm) with MBP staining depicted in green and QD9 staining in red. (D) Magnification of caudal corpus callosum marked by the white box in (C). Quantification of the absolute staining intensity with QD9 (E) and MBP (F) over cuprizone time course. (G) Quantification of the ratio of the staining intensities of MBP and QD9. All graphs show the mean with SEM (n=3 animals, 3-5 regions of same size per animal, *=p<0.05, **=p<0.01, ***=p<0.001, ANOVA).

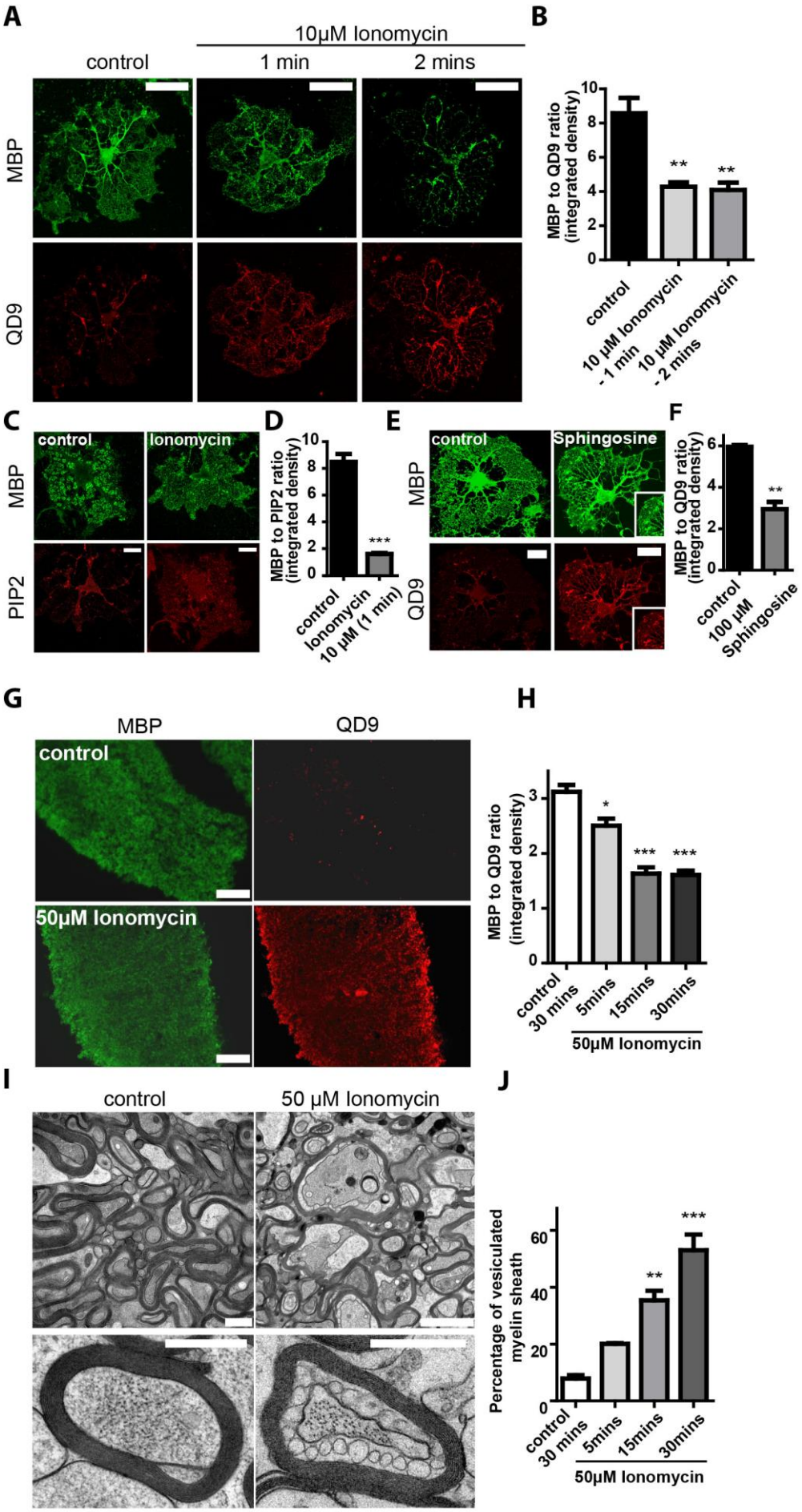
A
10μM Ionomycin
control
1 min
2 mins
MBP
QD9
B
MBP to QD9 ratio (integrated density)
control
10 μM Ionomycin - 1 min
10 μM Ionomycin - 2 mins
C
control
Ionomycin
MBP
PIP2
D
MBP to PIP2 ratio (integrated density)
control
Ionomycin 10 μM (1 min)
E
control
Sphingosine
MBP
QD9
F
MBP to QD9 ratio (integrated density)
control
100 μM Sphingosine
G
MBP
QD9
control
50μM Ionomycin
H
MBP to QD9 ratio (integrated density)
control
30 mins
5mins
15mins
30mins
50μM Ionomycin
I
control
50 μM Ionomycin
J
Percentage of vesiculated myelin sheath
control
30 mins
5mins
15mins
30mins
50μM Ionomycin

Figure S3. Epitope unmasking after loss of membrane binding, related to Figure 4. (A) Treatment of primary mouse oligodendrocytes at DIV 5 with the calcium ionophore ionomycin (10 µM, 1 or 2 mins) and subsequent immunostaining for MBP in green and with QD9 in red. (B) Quantification of the MBP to QD9 ratio of integrated density (n=3, >80 cells per condition, **=p<0.01, one-way ANOVA). (C) Representative images of MBP staining in green and PIP2 stain in red of oligodendrocytes at DIV 5 after 10 µM ionomycin treatment for 2 mins. (D) Quantification of the MBP to PIP2 ratio of integrated density (n=3, >80 cells per condition, ***=p<0.001, Student's t-test). (E) Images representative of oligodendrocytes at DIV 5 after treatment with 100 µM sphingosine for 5 mins stained for MBP in green and QD9 in red (zoom in in the white box, scale bar 25 µm) and in (F), the quantification of the MBP to QD9 ratio of the integrated density (n=3, >80 cells per condition, **=p<0.01, ***=p<0.001, Student's t-test). All graphs show the mean with SEM. (G) Acute brain slices of mouse brains were treated with 50 µM ionomycin in aCSF and subsequently stained with MBP (green) and QD9 (red) (scale bar 200 µm). (H) Quantification of the MBP to QD9 integrated density ratio (n=3 animals, 3-5 regions of same size per animal,***=p<0.001, Student's t-test). (I) Representative electron micrographs of high-pressure frozen samples after 30 mins ionomycin treatment (scale bar 500 nm). (J) Quantification of percentage of vesiculated myelin sheaths over ionomycin treatment time course (50 µM, 5 to 30 mins). Bars shown mean with SEM (n=3 animals, >200 axons per animal, ***=p<0.001, one way ANOVA).

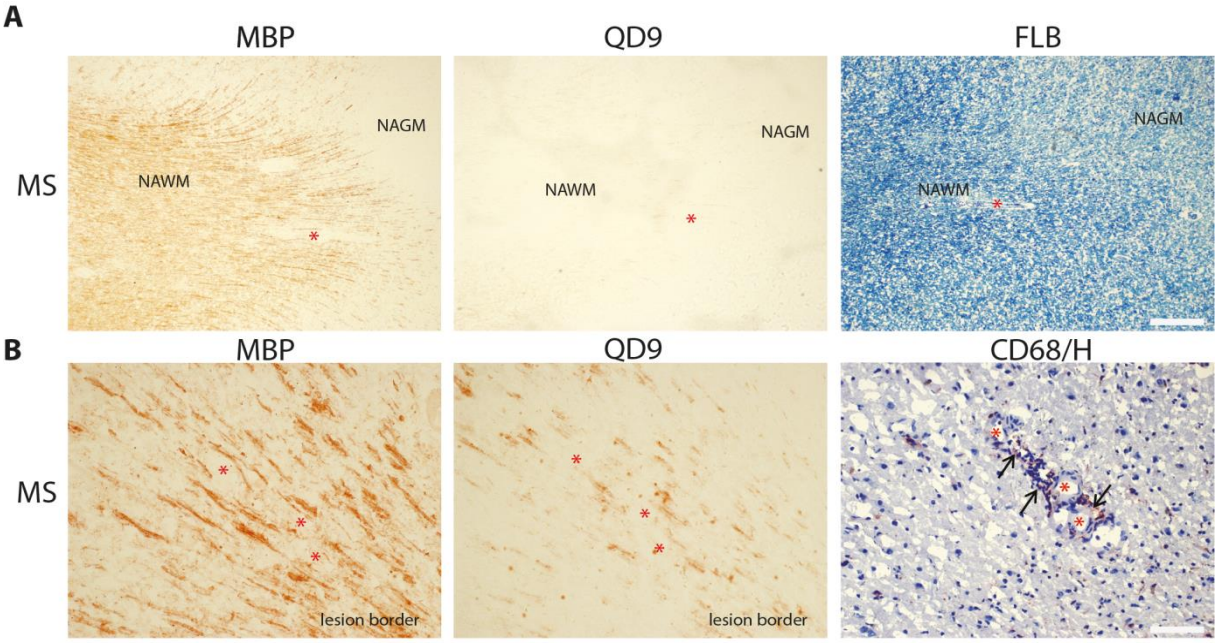

Figure S4. QD9 stains border zone around chronic white matter lesions, related to Figure 4. Representative images of myelin stains at the interface of subcortical white to cortical grey matter in multiple sclerosis; both panels depict anti-MBP IHC, anti-QD9 IHC and LFB for myelin in (A) and CD68 counterstained with hemalaun (H) in (B). (A) Images demonstrate that MBP-positive fibers in normal appearing white matter (NAWM) are not stained by the QD9 antibody. (B) Lesion border of a chronic active white matter lesion at higher magnification of the same MS case in an adjacent gyrus. Single QD9-positive fibers can be detected in proximity to CD68-positive cells (arrows). Scale bars: in a= 500 µm; in b= 100 µm. Blood vessels are indicated by asterisks. Abbreviations: Luxol Fast Blue, LFB; NAWM, normal appearing white matter; NAGM, normal appearing grey matter.

Supplemental Experimental Procedures:

Experimental autoimmune encephalomyelitis (EAE)
Biozzi ABH mice were obtained from Harlan UK Ltd. (Bicester, UK). Mice were injected subcutaneously with 50 µg recombinant MOG emulsified in complete Freund's adjuvants (CFA) on d0 and d7. Furthermore, the animals received an i.p. injection of 50 ng pertussis toxin (PTX) (List Biological Laboratories, Campbell, USA) on d0, d1, d7 and d8. The animals were scored daily for the development of paralytic disease and processed for electron microscopy at the peak of the first relapse.

Cuprizone treatment
For cuprizone time course studies, eight week old, male wild type (WT) C57B6N mice were fed with 0.2 % cuprizone (Sigma-Aldrich, Munich, Germany) in powered chow18. The animals were weighed once per week and if the body weight dropped below 20 % of the starting weight, the animal was euthanized. The animals were treated for a maximum of 5 weeks, and every week, one set of animals was perfused for histological studies, whereas the other set was processed by high pressure freezing for electron microscopy.

Acute slices of lesion site of AQP4 antibody injected Lewis rats
After injection of Lewis rats with AQP4 antibody and complement, rats were decapitated. Coronal slices were cut using a Leica VT1200S Microtome (Leica) at 200 µm thickness in ice-cold cutting solution containing the following: 130 mM NaCl, 3.5 mM KCl, 10 mM MgSO4, 0.5 mM CaCl2, 1.25 mM NaH2PO4, 24 mM NaHCO3, and 10 mM glucose with pH 7.4. Acute slices were allowed to recover in artificial CSF (aCSF) containing 148.2 mM, NaCl, 3.0 mM KCl, 1.4 mM CaCl2, 0.8 mM MgCl2, 0.8 mM Na2HPO4 and 0.2 mM NaH2PO4) at 35°C for 1h. The slices were then treated with 25 mM EGTA in aCSF or aCSF alone for 2h at RT. ACSF was continuously bubbled with carbogen (95% O2 and 5% CO2) gas. The acute slices were then fixed with 4% PFA and subsequently stained with guinea pig GFAP (Synaptic Systems) to identify the lesion site, mouse QD9 (Abcam) and rabbit MBP (Dako).
For treatment with ionomycin, the recovered slices were incubated in 50 µM ionomycin (dissolved in aCSF) at 35°C for 5 to 30 mins. Afterwards, the sections were processed for immunohistochemistry or for electron microscopy.

Immunoelectron microscopy
Immunoelectron microscopy was carried out as described previously (Werner et al., 2007). The brain sections were immersion fixed in 4% PFA with 0.25% glutaraldehyde, after infiltration with 2.3 M sucrose overnight, mounted on aluminium pins and snap-frozen in liquid nitrogen. The ultrathin cryosections were cut with a Leica UC6 cryoultramicrotome (Leica, Vienna, Austria) using a cryoimmuno diamond knife (Diatome, Biel, Switzerland).
The immunolabeling was performed as described previously (Peters and Pierson, 2008) using anti-MBP (Dako, rabbit, 1:300) or anti-PLP A431 (Sigma-Aldrich, rabbit, 1:250). The rabbit antibody was detected using protein A gold (10 nm, CMC, Utrecht, Netherlands) at a dilution of 1:20 for 20 min. The sections were imaged with a LEO912AB electron microscope (Zeiss, Oberkochen, Germany) equipped with a 2k CCD camera (TRS, Moorenweis, Germany). The quantification of the labels was on >70 axons, where the gold particles for the compact myelin were counted and divided by the label obtained in vesiculated myelin.

Antibodies, plasmids and other reagents
The following antibodies were used in this study: mouse monoclonal IgG anti-MBP (Sternberger, Lutherville, USA), mouse monoclonal IgG QD9 (Abcam, Cambridge, UK), rabbit polyclonal IgG anti-MBP (Dako, Carpinteria, USA), rabbit polyclonal IgG anti-myc tag (Sigma-Aldrich, Munich, Germany), mouse monoclonal IgG anti-CD68 (Abcam, Cambridge, UK). Secondary antibodies conjugated with fluorophores or horseradish peroxidase were purchased from Dianova (Hamburg, Germany). Biotinylated secondary antibodies were purchased from Jackson Immuno Research Europe ltd. (Suffolk, UK).
Ionomycin was purchased from Calbiochem (Darmstadt, Germany).

Cell culture, transfections and treatments
Primary cultures of mouse oligodendrocytes were prepared from postnatal day zero (P0) mice as described previously (Trajkovic et al., 2006). In brief, the oligodendroglial progenitor cells growing on top of a monolayer of astrocytes were obtained via differential shaking. After their harvest, the cells were cultured on PLL-coated dishes or coverslips with minimum essential media containing B27 supplement, 1% horse serum, L-thyroxine, glucose, glutamine, penicillin, streptomycin, pyruvate and bicarbonate (SuperSato-B27).
Treatment of the oligodendrocytes DIV 5 was carried out with 10 µM ionomycin in Krebs-Ringer solution (120 mM NaCl, 4.7 mM KCl, 10 mM glucose, 20 mM HEPES, 1.2 mM $CaCl_2$, 0.7 mM $MgSO_4$, pH 7.4) by first

washing the cell layer in Krebs-Ringer without $CaCl_2$ and then incubating with 10 µM ionomycin for 1-2 min in Krebs-Ringer with $CaCl_2$.
Treatment of oligodendrocytes at DIV 5 with 100 µM sphingosine was carried out for 5 min in serum-free media. The viability of the cells was assessed using the MTT assay.
Cells were fixed after treatment or transient transfection with 4% PFA with 0.25% glutaraldehyde and stained with MBP and QD9 or PIP2 or CNP.
PtK2 cells were cultured in DMEM with 4.5 g/L glucose supplemented with 10 % FCS, 2 mM GlutaMAX, 1 mM pyruvate and 50 units/mL of penicillin and streptomycin. The adherent cells were split on a regular basis with 0.05% trypsin-EDTA. For transient transfections, the TransIT-LT1 transfection reagent (MoBioTec, Göttingen, Germany) was used according to the manufacturer's protocol.

Immunofluorescence and microscopy
Immunocytochemistry was carried out was described previously (Trajkovic et al., 2006). All fluorescent images were acquired at the Leica DMI6000 fluorescence microscope equipped with a 20x NA 0.40 and 40x NA 0.60 dry plan-apochromate objective; or Leica TCS SP2 AOBS confocal microscope (Leica Microsystems, Mannheim, Germany) equipped with a 40X NA 1.25 and 63X NA 1.40 oil plan-apochromat objective or Leica TCS SP5 AOBS confocal laser scanning setup (Leica Microsystems, Mannheim, Germany) with a 40X NA 1.25 and 63X NA 1.40 oil plan-apochromat objective. At least, three independent experiments were performed for each analysis. For experiments employing cells, at least 20 cells were imaged per condition. For immunohistochemistry, at least 3 areas per animals with 3 animals per experimental condition were assessed. The images were processed and analyzed using the public domain Java-based image processing software ImageJ (created by W.S. Rasband, National Institutes of Health, Bethesda, Maryland, USA) by determining the signal intensity and the integrated density (area multiplied by the signal intensity).

Immunohistochemistry
Animals for immunohistochemistry were perfused after with ice-cold filtered PBS followed by freshly prepared filtered 4% PFA in PBS. The tissues were immersion-fixed overnight in 4% PFA and 1% PFA prior to cryoprotection in 30% sucrose. After embedding, the tissues were cut using the Leica cryostat CM1850 and stored in cryoprotective solution (25% glycerol, 25% ethylene glycol in PBS) at -20°C. Sections for immunofluorescence were either processed free-floating after washing with PBS (thrice for 30 min) The samples were permeabilized with 0.5% Triton X-100 in PBS for 1 h at room temperature (RT) and then, blocked in 5% horse serum, 5% goat serum and 5% fetal calf serum in 0.5% Triton X-100 (blocking solution) for 1 h at RT. For tissue injected with an human antibody, blocking with 1:100 dilution of goat anti-human IgG and IgM (Dianova, Hamburg, Germany) in blocking solution was carried out for 1 h at RT. The sections were incubated with the desired primary antibodies in appropriate dilution in blocking solution overnight. Primary antibodies used were polyclonal rabbit anti-MBP (Dako, Carpinteria, USA) and mouse monoclonal QD9 antibody (Abcam, Cambridge, UK) or mouse monoclonal MAG antibody (Millipore, Billiceria, USA). The sections were washed and incubated with the secondary antibodies conjugated with Alexa Fluor 488 or Alexa Fluor 555 and the nuclear counterstain DAPI for 1 h at RT. After washing the sections, they were mounted using mowiol and dried.

Immunohistochemistry of human tissue
MS and control brain tissue samples were provided by the UK Multiple Sclerosis Tissue Bank (UK Multicentre Research Ethics Committee, MREC/02/2/39), funded by the Multiple Sclerosis Society of Great Britain and Northern Ireland (registered charity 207495). All brain tissues were routinely screened by a neuropathologist to confirm diagnosis of MS and to exclude other confounding pathologies.Immunohistochemistry of human brain tissues was performed on tissue sections from 6 tissue blocks from 4 MS cases and on 5 tissue blocks from 4 control cases. CNS tissue from 4 patients with serologically confirmed NMO or NMO spectrum disease obtained at biopsy was examined. Brain or spinal cord biopsy was performed for diagnostic purposes to exclude tumor, lymphoma or infection. The study was approved by the local ethics committee. All tissue blocks were fresh frozen within a post mortem-time of maximum 18 h and an average post-mortem time of 12 h. Cryostat sections of 12µm were mounted on Superfrost Plus glass slides, dried at room temperature (RT) and stored at -80°C. The slides were thawed for 15 mins at 4°C and then fixed in 4% fresh PFA for 5 minutes at RT. The sections were washed thrice in PBS for 5 minutes at RT (for all washes, unless stated otherwise). For the MBP and QD9 staining, a permeabilization was performed in 70% Ethanol in PBS overnight at RT. After washing, endogenous peroxidase activity was blocked with 0.06% hydrogen peroxide in PBS for 30 mins at RT (for CD68: 0.06% hydrogen peroxide and 80% methanol in PBS). The tissue sections were washed again and blocked in buffer containing 5% normal donkey serum and 0.05% Triton X-100 in PBS for 1h at RT (for CD68: 1% normal donkey serum, 0.1% Triton X-100 and 0.05% Tween-20 in PBS). The primary antibody was incubated overnight at 4°C in the following dilutions: MBP diluted 1:300, QD9 diluted 1:2000 and CD68 diluted 1:250 in blocking buffer. After washing the sections, the secondary antibody was added for 1 h at RT. The tissue sections were washed and the avidin biotin complex (PK6100-Standard, Vector Laboratories, Inc., California, USA) was added

to the sections as described by the manufacturer and incubated for 30 mins at RT. The sections were washed and incubated in a solution containing 3-Amino-9-ethylcarbazol (AEC), 0.125% glacial acetic acid and 0.03% hydrogen peroxide for 6 mins at RT. The sections were washed as above, then washed twice in distilled water for 2 mins, mounted with Aquatex and dried overnight. The tissue stained for CD68 was stained with hemalaun prior to washing in distilled water by bathing the slides for 15 secs (Papanicolaou Solution 1a Harris Hematoxylin solution, Merck Millipore) and then rinsing them under flowing tap water for 8 mins.

Statistical analysis

All data were expressed as means ± standard errors of the mean (SEM). Statistical analysis was conducted with Prism software (GraphPad Software Inc., La Jolla, CA). We used the Student t-test, one-way or two-way ANOVA as indicated and with post-tests as appropriate. The level of significance was set at $p < 0.05$. Single, double, and triple symbols denote statistical significance at the 0.05, 0.01, and 0.001 levels, respectively.

Supplemental References:

Peters, P.J., Pierson, J., 2008. Immunogold labeling of thawed cryosections. Methods Cell Biol. 88, 131–49. doi:10.1016/S0091-679X(08)00408-1

Trajkovic, K., Dhaunchak, A.S., Goncalves, J.T., Wenzel, D., Schneider, A., Bunt, G., Nave, K.-A., Simons, M., 2006. Neuron to glia signaling triggers myelin membrane exocytosis from endosomal storage sites. J. Cell Biol. 172, 937–48. doi:10.1083/jcb.200509022

Werner, H.B., Kuhlmann, K., Shen, S., Uecker, M., Schardt, A., Dimova, K., Orfaniotou, F., Dhaunchak, A., Brinkmann, B.G., Möbius, W., et al., 2007. Proteolipid protein is required for transport of sirtuin 2 into CNS myelin. J. Neurosci. 27, 7717–30. doi:10.1523/JNEUROSCI.1254-07.2007